We are IntechOpen, the world's leading publisher of Open Access books Built by scientists, for scientists

4,800
Open access books available

122,000
International authors and editors

135M
Downloads

Our authors are among the

154
Countries delivered to

TOP 1%
most cited scientists

12.2%
Contributors from top 500 universities

WEB OF SCIENCE™

Selection of our books indexed in the Book Citation Index in Web of Science™ Core Collection (BKCI)

Interested in publishing with us?
Contact book.department@intechopen.com

Numbers displayed above are based on latest data collected.
For more information visit www.intechopen.com

2

Joint Torque Sensory in Robotics

Farhad Aghili
Canadian Space Agency
Canada

1. Introduction

Joint Torque sensory Feedback (JTF) can substantially improve the performance of a robotic system. JTF makes it possible to achieve dynamic control of a robotic manipulator without the need for modeling its link dynamics. Moreover, it has been proved that JTF can achieve a precise torque tracking in a manipulator joint by compensating the effect of joint friction and actuator nonlinearities. Despite these advantages, accurate joint torque measurement encounters several practical challenges. Since much of the torque/force reaction of the link load on the joints appears in the form of nontorsional components, e.g. overhung force and bending moment, the torque sensing device has to not only bear but remain insensitive to these force/moment components. In addition, it is desirable to design the structure of the sensor such that it generates a large strain for a given load torque and therefore has a high sensitivity. However, this is in conflict with the high-stiffness requirement for minimizing the joint angle error introduced by the sensor.

The main objectives of this chapter are twofold: Firstly, in Sections 2 and 3, we describe the technical challenges and practical solutions to accurate measurement of joint torques in the presence of the non-torsional components in a robot joint. For a torque sensing device, different mechanical structures will be examined and their properties, such as sensitivity and stiffness in different directions and decoupling, will be explored. This allows a systematic design of a sensor structure which is suitable for torque measurement in a robot joint. Finally, the state-of-the-art and design of a torque sensor for robots will be presented in Section 4. The design achieves the conflicting requirements of high stiffness for all six force and torque components, high sensitivity for the one driving torque of interest, yet very low sensitivity for the other five force/torque components. These properties, combined with its donut shape and small size make this sensor an ideal choice for direct drive robotic applications. Experimental data validates the basic design ideas underlying the sensor's geometry, the finite element model utilized in its optimization, and the advertised performance.

The second objective is to describe the application of joint torque sensory feedback (JTF)in robot control. The main advantages claimed for JTF are (i) it can simplify the complexity of the system dynamics by eliminating its link dynamics; and (ii) the control system is inherently robust with respect to both external force disturbance and parameter variation. First, assuming both actuator and torque sensor are ideal, we describe robot control with JTF in Section 5. Then, development of an adaptive JTF is presented in Section 6that requires only the incorporation of uncalibrated joint torque signals, i.e., the gains and offsets of multiple sensors are unknown. Also, all physical parameters of the joints including inertia of the rotors, link twist angles, and friction parameters are assumed unknown to the

Source: Industrial Robotics: Programming, Simulation and Applicationl, ISBN 3-86611-286-6, pp. 702, ARS/plV, Germany, December 2006, Edited by: Low Kin Huat

controller. Finally, in Section 7, JTF is modified to cope with actuator's finite bandwidth dynamics actuator, i.e., no ideal actuator. An optimal JTF is designed in the frequency domain that minimizes the control system's sensitivity to load torque disturbances and load dynamics. Experimental results demonstrate that the JTF remarkably improves the disturbance attenuation and load decoupling properties of a joint servo controller.

2. Sensing Joint Torque

The benefits of using joint torque sensory feedback to improve the performance of robotic system have been recognized in the robotics community. For example, joint torque feedback can be used to compensate the nonlinearities and modeling uncertainties of manipulator dynamics (Hashimoto, 1989a; Kosuge *et al*., 1990;Aghili *et al*., 2001) or simply those of actuators (Asada and Lim, 1985; deSilva *et al*., 1987; Zhangand Furusho, 1998; Luh *et al*., 1983). Moreover, in geared systems, the implementation of model based controllers is difficult without measuring the actual output torque, since the efficiency of gears depends greatly on the torque, and to a lesser extend, on the joint velocity, and yet this data is typically not made available by gear manufacturers. Thus there is a need for torque sensors that can be integrated simply between the actuator (and possibly gear) and the load. The sensor research described in this section was motivated by the lack of suitable sensors needed for our joint servo system.

Accurate joint torque measurement encounters several design challenges. In the design of robot manipulators, it is desirable that much of the torque/force reaction of the link load on the joints appears in the form of non-torsional components, because actuation then takes less effort. SCARA robot arm designs, for instance, prevent gravity torques from acting on the joint motors (Newman and Patel, 1991). However, since torque sensors are directly attached to the motor's distal links, they have to bear those potentially large non-torsional components. The first challenge is to measure torque with minimal influence from simultaneous and potentially large non-torsional components. In the following, we shall call the one axis of motor torque of interest the torsion. The other two torque and three force components, we shall call for simplicity the non-torsional components. The second challenge relates to the sensor stiffness. High torsion stiffness is important because any deflection adds positioning errors that cannot be compensated by the joint servo controller. To increase the signal-to-noise ratio and sensitivity of the sensor, it is desirable to design a structure that generates a large strain for a given load torque. However, the sensitivity introduces a torsion compliance that must be minimized. Thus there are two conflicting requirements: High stiffness and high sensitivity for torsion. A new solution to these two challenges will be described here and is distinct from existing designs. Some aspects of this research have been previously reported in (Aghili *et al*., 2002a).

There is a large literature on the systematic design of six degree-of-freedom (dof) force/torque sensors (Hirose and Yoneda, 1990;Svinin and Uchiyama, 1995;Uchiyama *et al*., 1991). It is important to note that the design criteria for one and six dof sensors are very different. For instance, isotropy (uniform sensitivity)is a desirable property of a six degree-of-freedom force/torque sensor, hence its elastic structure tends to be fragile and compliant in all directions. In contrast, the elastic sensitivity of a torque sensor has to be maximized only around its torsional axis.

Various techniques have been proposed to instrument geared motors for torque sensing (Hashimoto, 1989b; Luh *et al*., 1983; Pfeffer *et al*., 1989; Vischer and Khatib, 1995), while little attention has been paid to find an adequate structure for joint torque sensing (Asada

and Lim, 1985; Jacobsen *et al*., 1991; deSilva *et al*., 1987). Hashimoto *et al*. (Hashimoto, 1989b) utilized the elasticity of the flex-spline in a harmonic drive to measure the joint torque. This technique has the advantage of using the existing structural flexibility of the robots. However, eliminating the error caused by rotation of the wave generator is difficult, it requires a nontrivial gear modification, and this approach cannot be used in direct drive systems. Many researchers (Pfeffer *et al*., 1989; Wu, 1985;Luh *et al*., 1983;deSilva *et al*., 1987; Asada and Lim, 1985; Vischer and Khatib, 1995) choose not to place the sensor directly at the joint shaft to avoid the detrimental effects of the support forces and moments. Pfeffer *et al*. (Pfeffer *et al*., 1989) replaced standard attachment bolts in the PUMA 500 joints with a flexure instrumented with strain gauges. Wu (Wu, 1985) used a shaft with a thin hollow circular section that is supported by two bearings. Strain gauges are mounted on the thin section. Luh *et al*. (Luh *et al*., 1983) cemented strain gauges on the connecting output shaft which is mounted to the flex-spline of the harmonic drive for each joint of the Stanford manipulator. Visher (Vischer and Khatib, 1995) integrated a torque sensor with the gear transmission, while Asada et al. (Asada and Lim, 1985) integrated strain gauges in the hub supporting the robot of a direct-drive motor. The strain gauges are cemented on three beams connecting the outer ring, mounted to the motor rotor, and the inner ring, which is coupled to the motor shaft. Asada et al. (Asada and Lim, 1985) cemented strain gauges inside the rotor of a direct-drive motor for torque measurement. Since these sensors are not mounted directly on the joints of a manipulator, the entire set of forces and moments are supported by the bearing set rather than the sensor structure. However, these sensors are not ideal because they can not account for the friction in the joint bearings. Moreover, the mechanical joints are complicated and sometimes bulky. In commercial torque sensors non-torsional components are not permitted or are highly restricted. Furthermore, they usually come in bulky packages, are built for shaft mounting and thus are not suitable for integration in a robot joint.

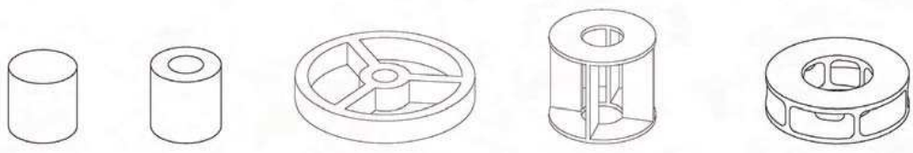

Fig. 1. Different structure for torque sensor.

Fig. 1 illustrates conventional geometries (a, b, c, and d) and the proposed hollow hexaform design (e) for torque sensors. Solid (a) and hollow (b) cylinders have been used extensively for joint torque sensing (Pfeffer *et al*., 1989; Wu, 1985; Luh *et al*., 1983; deSilva *et al*., 1987; Wu and Paul, 1980) but are sensitive to non-torsional components (Wu and Paul, 1980). For this reason, they are usually mounted before the joint bearings so that the bearing can support the non-torsional components. In addition to requiring a bearing support structure, the main drawback of this method is that joint friction can not be observed by the sensor. Hub-sprocket designs Fig.1(c) have been used for geared joints (Hirzinger *et al*., 2001; Vischer and Khatib, 1995) as well as direct-drive joints (Asada and Lim, 1985; Tani *et al*., 1983). Although a better rejection

to non-torsional components has been reported for this type of sensor (Vischer and Khatib, 1995), the structure is not adequate for a modular robot joint. This is because of the drastic change in the physical size between the input (inner ring) and output (outer ring) of the sensor. Rather this type of sensor should be integrated with the gear or with the rotor of a direct-drive motor, and hence it suffers from the same drawbacks as type (a) and (b) sensors.

The hollow cruciform design Fig. reffig: quad is used in commercially available torque sensors (Lebow, 1997). In this design, strain is induced mainly by bending of the wing elements. In order to achieve good sensitivity, the wing and sensor height is large, and as a result, the stiffness is low and non-torsional torques must be kept small. The proposed hollow hexaform sensor Fig. 1(e) is similar in its basic geometry to the hollow cruciform sensor (d) with only four wings. However, there are fundamental functional differences. Due to the increased number of wing pairs, and the shorter height, strain is induced primarily in torsion, resulting in a much stiffer sensor, and improved sensitivity. In addition, this design can be optimized to support non-torsional torques, making it suitable for direct drive robotic applications.

3. Sensor Design

In this section we describe how the new hollow-hexaform sensor achieves

(i) high sensitivity to torsion,
(ii) low sensitivity to non-torsional components, and
(iii) high stiffness in all axes of forces and moment.

3.1 Design for Decoupling

In general, torque measurements are derived from strain measurements at several locations on an elastic sensor body. Assuming a linearly elastic material, there is a linear relationship between the applied forces and torques and the resultant strains described by

$$\epsilon = C\, f, \tag{1}$$

where $\epsilon \in \mathbb{R}^m$ is the vector of m measured strains, $f \in \mathbb{R}^6$is the generalized force/moment vector acting at the center of the sensor body where the z-axis and joint axis are identical, and $C \in \mathbb{R}^{m\times 6}$is the sensitivity matrix whose elements c_{ij} denote the sensitivity of the *i*th strain gauge to the *j*th component of the generalized force/moment. This matrix permits the reconstruction of the torsion moment from the output signal with the gain vector. Unlike in 6-axis force/torque sensors, it is desired to reconstruct only the torsion moment n_z from the measured strains ϵ. However, the sensitivity matrix underlies the mechanical coupling transmitted through the force/moment sensor structure. Therefore, the sensor output should be decoupled from the non-torsional components of forces and moments. We show that one can use the additive properties of the Wheatstone bridge to achieve the decoupling without the need for any subsequent arithmetic. The resulting advantage is a reduction of instrumentation and the number of wires by completing the bridge wiring inside the sensor, and simplification of tedious calibration.

The question arises concerning the condition for which there exists such a mapping. It is necessary to consider each component of force to be a linear function of all strain gauge sensors in order to correct for the coupling. Let v_{out} and v_{ex} represent the output voltage and the excitation voltage of a half-bridge configuration, and GF denote the gauge factor

(Omega, 1995) of the strain gauges. Then, assuming every strain gauge pair constitutes a half-bridge circuit, the overall voltage output is given by $v_{\text{out}} = \kappa t^T \epsilon$ where $\kappa = 0.5GFv_{\text{ex}}$ is the gain of the strain gauges and $t = [-1, 1, -1, 1, \cdots]^T$ represents the gain signs corresponding to the negative and positive branches of a Wheatstone bridge circuit. Substituting ϵ from (1) into the latter equation, we obtain

$$v_{\text{out}} = \kappa t^T C f = \kappa \sum_{i=1}^{6} w_i f_i, \tag{2}$$

where w_i is the inner product of vectors t and the ith column of C. It is evident from (2) that, in the most general case, the sensor output is the superposition of weighted components of the generalized forces and moments transmitted through the sensor unless all weights related to the exogenous forces and moments are zero. That is, the decoupling is achieved if $w_1 = \cdots = w_5 = 0$ and $w_6 \neq 0$. In this case, the sensor output is solely proportional to the torsion torque $\tau_J = f_6$,i.e.,

$$v_{\text{out}} = \alpha \tau_J, \tag{3}$$

where $a = \kappa w_6$ represents the overall sensitivity of the sensor. That vector t is orthogonal to all columns of C matrix except the last one underlines a condition on the structure of a torque sensor by which the senor exhibits the decoupling. As a results, such as sensor is not sensitive to the supporting forces and moments transmitted through the structure of the sensor.

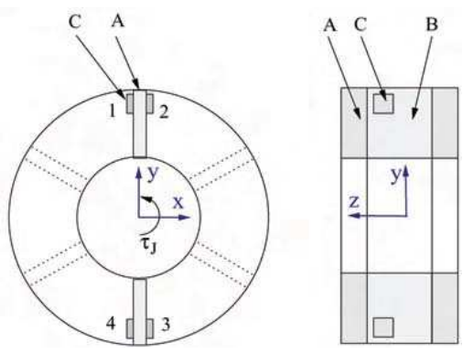

Fig. 2. Basic torque sensor structure. A: solid discs; B: elastic element; C: strain gauge.

For the candidate geometry in Fig. 2andwith four strain gauges located on the numbered locations, the parametric form of the sensitivity matrix can be derived from the symmetry of the structure with respect to the external forces and torques as

$$C = \begin{bmatrix} c_{11} & c_{12} & c_{13} & c_{14} & c_{15} & -c_{16} \\ c_{21} & c_{12} & c_{13} & c_{14} & -c_{15} & c_{16} \\ c_{21} & c_{32} & c_{13} & -c_{14} & -c_{15} & -c_{16} \\ c_{11} & c_{32} & c_{13} & -c_{14} & c_{15} & c_{16} \end{bmatrix}.$$

The jth column of the matrix represents the strain sensitivities in the four site locations with respect to the jth load case, e.g., the third column represents the sensitivity due to f_3.The identical elements in the matrix can be implied from the symmetric configuration of the structure with respect to different load cases. For instance, the symmetric condition of the

strain gauges with respect to the axial load, f_3, implies identical elements of the third column. Now one can readily verify that $w_1 = \cdots = w_5 = 0$ and $w_6 = 4c_{16}$ and hence the structure satisfies the condition for mechanical decoupling.

There are two main reasons in practice that violate the above assumption of exact symmetry among the measured strains. First, strain gauges exhibit variations in their gauge factor. Second, the strain gauges will be placed on areas with high strain gradients. This makes the gauge outputs sensitive to placement errors. This can also be modeled as a gauge gain error. As a consequence, exact cancelation of the non-torsional components may not be achieved with the theoretical gain vector. By virtue of the linear mapping (1), the non-torsional components produce no output, if all elements of the sensitivity matrix except that for the last column are sufficiently small. This implies that the strain sensitivity to the non-torsional components has to be held to a minimum by mechanical design. This condition in conjunction with the decoupling property of the sensitivity matrix actually determines the capability of the sensor to reject the effect of non-torsional force/torque to the output and to provide a high fidelity output signal.

3.2 Maximum sensitivity

To increase the signal-to-noise (S/N) ratio and the resolution of the sensor, it is desirable to design the elastic component to provide large output signals, i.e., large mechanical gain α. Therefore one of the design criteria is to increase the torsional sensitivity, subject to not exceeding the allowable strain. In the absence of non-torsional components, the maximum attainable strain sensitivity depends solely on the material properties as the strain due to the maximum load should be close to the maximum allowable material strain or stress. However, non-torsional components produce strains which add to the strain caused by torsion. To ensure that the allowable maximum material strain is not exceeded, we consider the worst-case scenario where the generalized force/torque vector has its maximum force and moment. Then, in order to exploit maximum torsion sensitivity, c_{16}, the other sensitivity components, i.e. $\{c_{11}, \cdots, c_{15}\}$, must be minimized by proper geometry design. This design requirement is consistent with a decoupling property of the sensor. It is interesting to note that cylinders are mainly used in the design of commercial torque sensors. By elementary strength of material analysis, one can show that bending moments produce twice the stress than the same magnitude torsion moment. This is why shear and thrust forces and bending moments must be kept small in these sensors.

3.3 High torsional and bending stiffness

Torsional deflection degrades the position accuracy of the joint angle controller. Moreover, to increase the signal-to-noise ratio requires maximizing the sensor sensitivity. However, highly stiff sensors tend to be less sensitive ones. Therefore, one of the critical design challenges is to maximize the stiffness while maintaining high sensitivity. We propose η, called structure efficiency, which is the product of sensitivity and stiffness as a performance index to capture these contradictory requirements,

$$\begin{gathered}\text{(torsional sensitivity) (torsional stiffness)} \\ = \frac{4\kappa\epsilon_1}{\tau_J} \cdot \frac{\tau_J}{\delta} = 4\kappa\frac{\epsilon_1}{\delta},\end{gathered} \tag{4}$$

where δ is the torsional deflection. As mentioned earlier, the gain of the strain gauge, κ, is

independent of sensor structure. Moreover, ϵ_1/δ is a dimensionless variable which captures the ratio of the local and global strains. These facts suggest that η is a decisive factor in the sensor design and should be maximized. Moreover, since it is dimensionless, the index provides a useful basis for comparison of different size torque sensors. The index is maximized in elastic structures that produce high strain concentration in torsion. In theory, there is no limit on the strain concentration in an elastic body. However, the high strain concentration takes place in a very small area, which might be smaller than the physical size of available strain gauges. Moreover, since strain gauges average the strain field over their area, the detected strain can be significantly lower than the calculated value. Therefore, it is important to generate high strain over a sufficiently large area. This objective seems difficult to formulate analytically, but can be inspected by finite element methods.

Introducing a torque sensor in a robot joint adds flexibility. Although torsional flexibility can, in principle, be compensated via sophisticated controllers, deflection in the other axes is more problematic. Consequently, another design criterion dictates high stiffness in non-torsional directions. Fortunately, the requirements for low deflection and low strain sensitivity for non-torsional components are consistent. The structure shown in Fig. 2 exhibits high bending stiffness around the x-axis. However, its poor stiffness around the y-axis is a drawback. This problem can be simply solved by adding more wing pairs as shown in Fig. 1E. This improves the uniformity of the bending stiffness along different axes as well as the body stiffness. In general, all performance aspects of the sensor improve with the number of wing pairs, but since we will want to machine the sensor from one solid piece of metal, the limit is imposed by manufacturability. For this reason, we consider six wings in our design.

3.4 Practical shape considerations

Addition of a torque sensor to a robot joint must not require the redesign of the joint and should result in a minimal change in the manipulator's kinematics, in particular the link offset. Hence, a shape with a small width is desirable. Minimizing the effects of thermal stresses is a design factor that cannot be ignored. Motors are a source of heat that flows from the motor to the attached link through the sensor body. Therefore, it is desirable to have an axisymmetric design that constrains the heat to flow in the axial direction, where no position constraint usually exists. The common hub-sprocket designs are prone to thermal stresses because of the temperature difference between the hub and the wheel. Since the sensor is specifically designed for a direct-drive motor with hollow shaft, flange mounting is preferred. Finally, the body should be designed for ease of manufacture. It should be a monolithic structure, that is, the body should be machined from a solid piece of metal. This decreases the hysteresis and increase the strength and repeatability of the sensor. The hollow hexaform geometry shown in Fig. 1E satisfies these requirements.

3.5 Material properties and overloading

So far only geometric properties of the elastic body were considered. Nevertheless, the stiffness and sensitivity characteristics of the torque sensor are also determined by the material properties. The maximum allowable strain for foil strain gauges is typically 3 %, which is at least one order of magnitude higher than that of industrial metals ϵ_{allow}, making the materials the limiting factor for sensitivity. Furthermore, the stiffness depends linearly on Young's modulus E of the material. By virtue of Hook's law,

$$\sigma_{\text{allow}} = E\,\epsilon_{\text{allow}}$$

one can conclude that high sensitivity and stiffness are achievable simultaneously only by use of a high-strength material.

Because a linear response is desired from the sensor, the chosen sensor material must have a linear strain-stress relationship. Steel is the best available industrial material that has good linearity properties within a large stress range. Moreover, due to the oscillatory nature of the loading, steel can work with in finite fatigue life as the allowable strains are determined based on the endurance limit. The endurance limit or fatigue limit is the maximum stress under which mechanical failure will not occur, independent of the number of load cycles. Only ferrous metals and alloys have an endurance limit.

The sensor is designed for a nominal torque 300 Nm that is based on the endurance limit of mild steel, which is twice as much as the yield point. Hence the safety factor in torque overloading is two. Remarkably, FEM results demonstrated that the stress induced by bending moment is very low for the proposed structure. As a result the structure can resist bending moments as high as 2000 Nm, which is almost an order of magnitude higher than the nominal torque.

3.6 Thermal deviation

The gauge resistance and gauge factor of all known strain sensitive materials vary with temperature. The change in resistance with temperature for a mounted strain gauge is a function of the difference in the thermal expansion coefficient between the gauge and the sensor body and of the thermal coefficient of resistance of the gauge alloy. Self-temperature compensating gauges can be achieved for specific materials by processing the strain sensitive alloy such that it has thermal characteristics that compensate for the effects of the mismatch in thermal expansion coefficients between the gauge and the body of the sensor (Omega, 1995). The manufacturer of the strain gauge (OMEGA (Omega, 1995)) claims that their products accurately compensate the effect of temperature if the yare chosen according to specific coefficient of thermal expansion of material on which the gauges are mounted.

4. Design and Analysis

4.1 FEM Analysis

Once we had determined the basic hollow hexaform shape of the sensor, we used the FEM capabilities of IDEAS (Structural Dynamics Research Corp.) to optimize the sensor dimensions and to determine the size and placement of the strain gauges. Strain concentration is the design key to simultaneously achieve high torsional sensitivity and high stiffness. For maximum sensitivity, strain gauges should be located where maximum induced strains due to the torsion load occur. Since the strain field is averaged over the area covered by the strain gauges, it is very important first to determine the loci of the peak strain, and second to ensure the creation of a sufficiently large strain field. FEM is ideally suited to solve this problem.

The sensor body is modeled by solid elements as shown in Fig. 3A. Since the body is symmetrical in geometry and applied boundary conditions, it suffices to analyze only one half, provided that adequate position constraints are imposed on the nodes of the cutting plane. To simplify the FEM, small geometric features of the body are suppressed. Several load cases were investigated, corresponding to axial and shear forces as well as bending and torsion moments.

In our application, the maximum forces and moments are 1000 N and 300 Nm,

respectively. A preliminary stress analysis showed that the axial and shear forces have negligible elastic effects because they produce a uniform strain/stress field in the elastic body, resulting in a very weak maximum strain. In fact, the bending moment is the critical non-torsional component, and consequently two different load cases corresponding to the external torsion and bending torques are established for FEM. It is important to note that in robotic applications the maximum angular deflection due to external torques (which is amplified by the robot links)is a more restrictive constraint than linear deflection due to the forces. It has been investigated that the worst-case strain due to the bending load happens when its axis lies perpendicular to one of the wings, and consequently that axis is chosen for the bending.

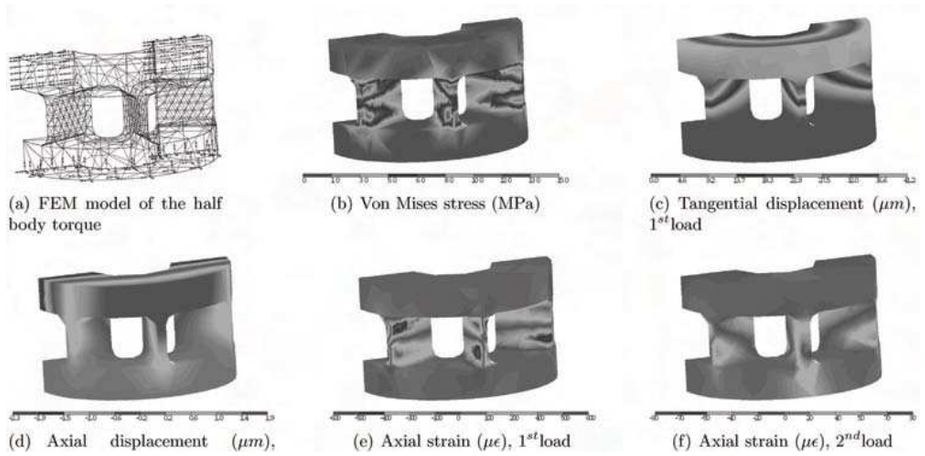

(a) FEM model of the half body torque

(b) Von Mises stress (MPa)

(c) Tangential displacement (μm), 1^{st}load

(d) Axial displacement (μm),

(e) Axial strain ($\mu\epsilon$), 1^{st}load

(f) Axial strain ($\mu\epsilon$), 2^{nd}load

Fig. 3. FEM analysis.

Moreover, as mentioned earlier, maximum torsional sensitivity requires minimum bending sensitivity. In particular, the radial displacement of the disc's outer diameter due to the torsion, principal strain at the strain gauge seats due to both load cases, and maximum von Mises stresses/strains due to a combination of all load cases are selected as the design benchmarks. The described design criteria can be checked with the FEM results to modify the geometry of the sensor iteratively.

In the shape optimization process we chose as design variables the wing thickness, the distance between two disks, and the inner hole diameter. The 95 mm outer diameter was selected to match our particular motor. The selected dimensions were varied to maximize the structure effciency (4) subject to keeping the maximum von Mises stresses σ within the allowable limits σ_{allow}, considering fatigue. That is

$$\max_{\text{design varibles}} \eta$$

$$\text{subject to} \quad \sigma < \sigma_{\text{allow}}$$

The IDEAS solver uses the Steepest Decent (the gradient method) method with penalty function for finding the local minimum - the penalty function adds simply the weighted constraint equation into the objective function.

The post-processing stage was guided by the following design benchmarks: the tangential

and axial displacement of the disc's outer diameter; the principal strain in the axial direction and parallel to the gauge axes, due to both load cases, and the maximum von Mises stress/strain due to a combination of all load cases. Hence, the performance index can be obtained from Figures 3(c) and 3(e), while the the constraint condition is given by Fig. 3(b). These design criteria were checked with the FEM results to modify the geometry of the sensor iteratively. The FEM results of the elastic body's final design are shown on Fig. 3. The worst-case von Mises stress, i.e. the combination of the two load cases, is shown in Fig. 3(b) where its maximum occurs at 150 MPa. This is close to the endurance limit of mild steel with a reasonable factor of safety. Figs 3(c) and 3(d) illustrate the tangential and axial displacement fields by which the torsional and bending stiffnesses are carried out; k_z =2.7 ×10^{5}Nm/rad and k_x =4.9 ×10^{6}Nm/rad, respectively. The axisymmetric pattern in the figure confirms the correctness of the imposed boundary conditions. Figs. 3(e) and 3(f) show the strain contour in the axial direction in which the strain gauges are oriented, for the 1st and 2nd load cases, respectively. The FEM results demonstrate that the strain sensitivity in torsion is seven times higher than in bending, while the bending stiffness is 18 times higher than the torsional stiffness

4.2 Experimental Characterization

The torque sensor was machined from a solid steel rod (Fig. 4). Foil strain gauges (SG-3/350-LY41 from Omega (Omega, 1995)) were cemented at the locations determined by FEM. The strain gauge bridge is excited by a precisely regulated 8.0 V DC voltage. Instrumentation amplifiers built into the sensor boost the signal level of the Wheatstone bridge output before A/D conversion. We took advantage of the hollow motor shaft, which is common in direct-drive motors, to locate the electronic circuit board beside the sensor. The local signal conditioning provides a stronger output signal and improves the S/Nratio. Moreover, since the electronic circuit is totally enclosed by the motor's hollow shaft, it is well shielded from the powerful magnetic noise created by the motor.

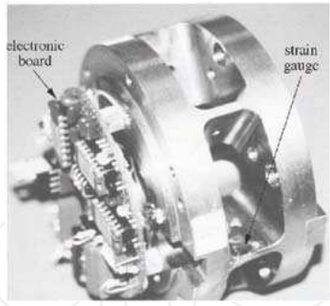

Fig. 4. The torque sensor prototype.

4.2.1 Static Test

In order to characterize the linearity and sensitivity of the sensor, static torsional and bending torques were applied in the experimental apparatus illustrated in Fig. 5. One side of the sensor is affixed to a bracket, while two aluminum bars were attached radially and axially to the other side. The ends of the bar were connected to a mechanical lever via ropes

in which load cells (MLP-50 from Transducer Techniques (Techniques, n.d.)) were installed. The lever varied the tension in the cord gradually between zero and maximum. During loading and unloading, the reference load cell output and the torque sensor output (device under test) were recorded.

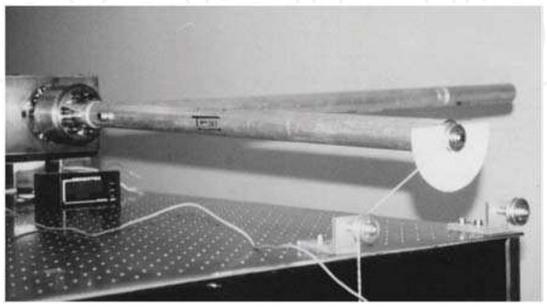

Fig. 5. The static test setup.

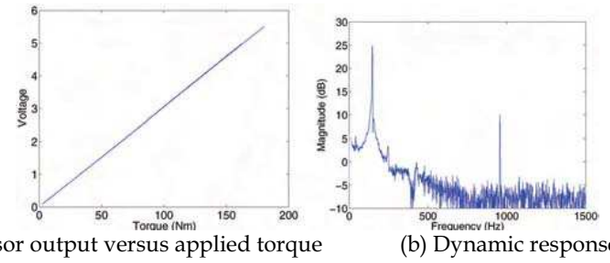

(a) Sensor output versus applied torque (b) Dynamic response

Fig. 6. Characteristics of the torque sensor.

The force transducer signal is scaled to torque and then is plotted versus the torque sensor output voltage in Fig. 6(a) for 2, 000 sample points. The slope of the line indicates the sensor calibration coefficient of α =30mV/Nm.The experimental data shows that all collective deviations from linearity are less than 0.2 % full scale.

Low sensitivity to the other axes is one of the key characteristic of a good joint torque sensor. The cross sensitivity measurements were performed by utilizing the static tesbed setup. Forces and moments are applied on different axes by the system of pullies and weights shown in Fig. 5. The bending moment is applied via an axial bar firmly connected to the sensor, while the torsion torque is applied by the radial arm. The direction of the force is set by a pulley, as shown in Fig. 5. Theoretically, the sensor output should not be responsive to the bending moment or the forces at all. However, in practice, due to inaccurate placement of the strain gauges and/or differences in the Gauge Factors of the strain gauges, exact decoupling may not be achieved. In the course of the experiment, it becomes evident that, with the exception of the torsion moment, the bending moment dominates the sensitivity of the sensor. The experimental result indicates that the ratio of the sensor readings with respect to the bending and torsion -the cross sensitivity -is only 0.6%. This confirms that the sensor effectively decouples the effect of the non-torsional components on the measured torque signal.

4.2.2 Dynamic Test

Dynamic testing serves mainly to validate the FEM results on which the stress analysis is based. The experiment is arranged to extract the stiffness of the sensor prototype. Again, the sensor is held rigidly by a bracket while a steel disk is flanged to the other side. The disk is massive, with an inertia of I_{zz} =0.24 kgm^2, and the whole system behaves like a second order system. To detect all the vibration modes corresponding to all compliance directions, the cross sensitivity is deliberately increased by electrically by-passing the strain of all strain gauge pairs except one. Therefore, the torque sensor no longer has the decoupling property, and its output is the summation of all torque/force components weighted by their corresponding gains. The system is excited impulsively by a hammer, and a data acquisition system records the subsequent vibration with a sampling rate of 3.2 kHz. Since the torsion gain is highest, the sensor signal is dominated by torsion vibration which decays due to the structural damping of the sensor material. Nevertheless, the sensor's modes are shown clearly in the frequency domain. To this end, a 0.5 second interval of the signal is taken via a Hamming window and then its spectrum is found by FFT. Fig. 6(b) reveals the modal frequencies associated with the bending and torsion compliances occurred at 150 Hz and 980 Hz. Due to the low damping, the modal frequencies are almost the same as the natural frequencies. The corresponding torsion stiffness is calculated to be k_z =2.4 ×10^{5}Nm/rad, which results in a high torsional stiffness. The bending stiffness can be found in the same fashion. However, it should be noted that the relative inertia is half of the inertia for disks, i.e. I_{xx} =0.5I_{zz}. The bending stiffness is calculated to be twenty times higher than the torsion stiffness, k_x =4.8 ×10^6 Nm/rad. A comparison with the FEM predictions reveals an acceptable 20% error.

5. Joint Torque Sensory Feedback

5.1 Motivation

Model-based robot control schemes have been proposed in the past for achieving precise motion tracking, e.g., resolved acceleration control (Luh *et al*., 1980), or the computed torque method (An *et al*., 1988). These approaches depend on dynamics modeling of the manipulator's load and link dynamics; they potentially perform poorly when the model is not accurate (An *et al*., 1988). Adaptive control of manipulators was proposed to deal with parametric uncertainties of the manipulator model (Slotine and Li, 1987). However, these controllers cannot deal with robotic systems with a unknown or variable payloads unless a more complicated adaptive versions is used (Yong-Duan *et al*., 1989). Robust control (Slotine, 1985) and robust adaptive control of manipulators (Reed and Ionnou, 1989) have been developed that can maintain the stability with respect to uncertainties, including bounded disturbance, time-varying parameters, as well as unmodeled dynamics. However, the performance may be compromised in these control approaches.

Alternatively, the dynamic control of manipulators can be performed by using joint-torque sensory feedback without the need for modelling link dynamics (Hashimoto, 1989b; Kosuge *et al*., 1990;Stokic and Vukobratovic, 1993; Aghili *et al.,* 2001; Aghili and Namvar, 2006). Such a controller can achieve robust performance against variation of link dynamics and rejection of external force disturbances at the expense of using additional sensors. Kosuge *et al*. (Kosuge *et al.,* 1990) demonstrated experimentally the effectiveness of using joint-torque measurements to compensate for the nonlinear link dynamics of a

SCARA-type direct-drive robot. Hashimoto (Hashimoto, 1989b) applied this technique to a harmonic-drive actuator where the deformation of flex-splines are used to measure joint-torques.

A survey of JTF can be found in (Stokic and Vukobratovic, 1993). In summary, the main advantages claimed for JTF are:

(i) Joint sensory feedback can simplify the complexity of a manipulator system dynamics by eliminating the link dynamics;
(ii) The control system is inherently robust w.r.t. parameter variation, e.g., a manipulator grasping a payload with mass variation; and
(iii) The control system can completely reject external force disturbances applied on the links.

It should be pointed out that essentially the joint torque measurement is possible if there is a small, but nonzero, joint deformation. A complete model of elastic-joint manipulators, which accounted for the dynamics of both the rotors of the drive system and the link system, were developed in (Murphy *et al*., 1990). These models were used by many researchers for development and analysis of non-adaptive (Spong, 1987; Tomei, 1991) and adaptive (Lozano and Brogliato, 1992) controllers for flexible joint manipulators. These controllers aimed at achieving high performance by taking finite stiffness of the joints into consideration; however, this complicates the equations of motion by increasing the order of the system. Tomei (Tomei, 1991) showed that even a simple PD controller, similar to that used for rigid manipulators, suffices to globally stabilize the elastic-joint manipulators about a reference point. The dynamics model developed in (Kosuge *et al*., 1990) for manipulators with JTF is a special case of the flexible joint model where the stiffness approaches infinity. Unlike the other control approaches, the JTF controller (Kosuge *et al*., 1990) requires only the rotor dynamics, i.e., a half-model. However, since the joint deformation is not compensated for by the controller, a sufficiently high joint stiffness is required so that the overall joint deformation can be assumed negligible.

5.2 Robot Dynamics with JTF

In robotics application, joint torque sensing can be used to eliminate completely the effect of link dynamics if the manipulator's joint are endowed with joint torque sensor device. The system dynamics are determined completely by the gyroscopic motion of the rotors of the joint actuators.

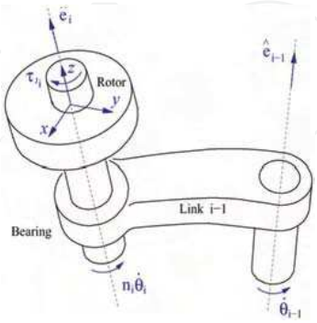

Fig. 7. The *i*th joint.

Fig. 7 depicts the *i*th motor axis and joint axis of a robot with n revolute-joints where each joint is driven by a geared motor with gear ratio n_i and assuming that the motor shaft is cut right at its junction to the link. In the following the subscript i denotes quantities related to the *i*th link or joint.

Assume that ω_{zi} be the z-component of the absolute angular velocity of the rotor ω_i; θ_i and $\bar{J}_i$ denote the rotor angle and the rotor inertia along the z-axis. Also, τ_{J_i}, τ_{M_i}, and $b_i(\dot{\theta})$denote the torques of the motor, the joint, and the bearing friction, respectively, all of them seen after the gearbox. Let us assume the followings: (i) The principal axes of all rotor inertias are parallel to their own joint axes; (ii) all rotors are statically balanced, i.e., their center of mass coincident with rotation axis; and (iii) the rotors are axisymmetric, i.e., their inertias about x and y axes are identical. Also as in (Kosuge *et al*., 1990), we assume that the deformation of the joint torque sensors are negligible. Moreover, let coordinate system $\{x_i, y_i, z_i\}$be attached to *i*th joint according to the Denavit-Hartenberg convention. Since the rotors are axisymmetric, the equation of motion of each rotor can be simply described by

$$J_i \dot{\omega}_{z_i} = \frac{1}{n_i}(\tau_{M_i} - b_i(\dot{\theta}_i) - \tau_{J_i}). \tag{5}$$

In the above equation, we need to obtain an expression for the absolute angular velocity in terms of joint angle quantities. Let $\hat{e}_j \in \mathbb{R}^3$represent a unit vector in the direction of the *j*th joint axis. Then, since the deformations of the torque sensors are assumed negligible, one can compute the link velocities by a technique similar to Luh *et al*. (Luh *et al*., 1980)

$$\omega_{i-1} = \sum_{j=1}^{i-1} \hat{e}_j \dot{\theta}_j, \tag{6}$$

$$\omega_{z_i} = \hat{e}_i^T \omega_{i-1} + n_i \dot{\theta}_i. \tag{7}$$

Equations (6) and (7) can be combined in the vectorial form as

$$\omega_z = (D(\theta) + N)\dot{\theta}, \tag{8}$$

where N =diag{n_i}, and $D(\theta) \in \mathbb{R}^{n \times n}$ is a lower triangular matrix whose elements are

$$d_{ij} = \begin{cases} \hat{e}_i^T \hat{e}_j & \text{if} \quad i > j \\ 0 & \text{otherwise} \end{cases}$$

It is worth pointing out that the unit vectors $\hat{e}_j$'s constitute the columns of the manipulator's rotation Jacobian (Sciavicoo and Siciliano, 2000), i.e. $A_\omega = \partial \omega_n / \partial q = [\hat{e}_1 \quad \hat{e}_2 \quad \cdots \quad \hat{e}_n]$.Hence, the D matric can be constructed from the Jacobian by

$$D = \text{tri}(A_\omega^T A_\omega),$$

where matrix function tri(.) returns only the lower-triangular elements of the input matrix, while the rest of elements of the returned matrix are zero. Defining $J \triangleq \text{diag}\{n_i^2 \bar{J}_i\}$and $T \triangleq I + N^{-1}D$, and using (8) in (5), we get

$$JT\ddot{\theta} + J\dot{T}(\theta, \dot{\theta})\dot{\theta} + b(\dot{\theta}) = \tau_{\text{net}}, \tag{9}$$

where $\tau_{\text{net}} = \tau_M - \tau_J$ is the net torque acting on the rotors.

Example. 1. *The coupling matrix D of a general 3-DOF robot is*

$$D(\theta) = \begin{bmatrix} 0 & 0 & 0 \\ ca_1 & 0 & 0 \\ ca_1 ca_2 & ca_2 & 0 \\ -sa_1 sa_2 c\theta_2 & & \end{bmatrix},$$

where a_1 and a_2 are the twist angles, and sa_i and ca_i represent sin(a_i) and cos(a_i).

Now, one can readily show that the following inverse-dynamics control scheme

$$\tau_{M_d} = \tau_J + u, \qquad u = JT(\theta)\left(\ddot{\theta}_d + G_D(\dot{\theta}_d - \dot{\theta}) + G_P(\theta_d - \theta)\right) + J\dot{T}\dot{\theta} + b, \tag{10}$$

where $G_D > 0$ and $G_P > 0$ are the feedback gains, can achieve dynamic tracking of the desired trajectory θ_d.

6. Adaptive Joint Torque Feedback with Uncalibrated Torque Sensor

In this section, we present development of an adaptive JTF controller that takes uncalibrated joint-torque signals, and then identifies the sensor calibration parameters as well as all joint parameters including rotor inertia, the link twist angles, and joint-friction parameters (Aghili and Namvar, 2006). We show that asymptotic stability of the proposed adaptive controller can be ensured if an upper bound on the estimated sensor-gain is respected. Subsequently, the parameter adaptation law is modified according to the projection parameter adaptation to meet the stability condition.

6.1 Adaptive Control

Note that dynamics formulation (9) is not adequate for an adaptive control because $J\,T$ is not a symmetric matrix. This problem can be fixed by changing the torque coordinate. Pre-multiplying (9) by $T(\theta)^T$ leads to

$$M_R\ddot{\theta} + h_R(\theta,\dot{\theta}) + b(\dot{\theta}) = T^T(\tau_M - \tau_J). \tag{11}$$

where $M_R = T^T JT$ and $h_R = C_R\dot{\theta} = T^T J\dot{T}\dot{\theta}$.

Remark. 1. *Since J is positive-definite and T is a nonsingular matrix, the symmetric inertia matrix M_R is positive-definite. Also, it can be readily verified that matrix $\frac{d}{dt}M_R - 2C_R$ is skew-symmetric.*

We assume that all joints are equipped with torque sensing devices and that vector $\tau_S \in \mathbb{R}^n$ represents the sensor outputs. Recall from (3) that the output signals are linearly related to the actual joint-torques. Hence, we can say

$$\tau_J = \alpha\tau_S + \beta, \tag{12}$$

where α =diag{a_i}and β^T =[β_1, , βn] are sensor gains and offsets, respectively. Substituting (12) in (11)gives

$$M_R\ddot{\theta} + h_R(\theta,\dot{\theta}) + T^T(b(\dot{\theta}) + \alpha\tau_S + \beta) = T^T\tau_M, \tag{13}$$

where the friction $b(\dot{\theta})$ can be captured by a friction model reported in the literature (de Wit et al., 1995).

The control objective here is to find a control law τ_M such that the rotor positions θ tracks the desired trajectory $\theta_d(t)$, while parameters *J, D, a, β* and friction coefficients are considered unknown. Moreover, note that the manipulators' twist angles are the only relevant parameters to matrix *D*. Hence, *T (θ, ρt)* can be parameterized in terms of the relevant kinematics parameters ρ_t –note that the kinematics parameters appear also independently in ρ_s in combination with dynamics and calibration parameters. Assume that the dynamics equation (13) is rewritten in a linearly parameterized form as

$$M_R\ddot{\theta} + C_R\dot{\theta} + T^T(b(\dot{\theta}) + \alpha\tau_S + \beta) \triangleq Y_s(\ddot{\theta},\dot{\theta},\theta,\tau_S)\rho_s, \tag{14}$$

where vector ρ_s contains combined dynamics, kinematics and calibration parameters. Now,

denoting $\hat{T}$, $\hat{\rho}_t$, $\hat{J}$, $\hat{C}$, $\hat{\alpha}$, $\hat{\beta}$, and $\hat{b}$ as the estimated variables, we propose the following control law

$$\tau_M = \hat{T}(\hat{\rho}_t)^{-T}(Y_s(\dot{v}, v, \theta, \tau_s)\hat{\rho}_s - Ls) \tag{15}$$

where

$$\begin{aligned} v &\triangleq \dot{\theta}_d - \Lambda(\theta - \theta_d), \\ s &\triangleq \dot{\theta} - v, \end{aligned} \tag{16}$$

and L > 0 and Λ > 0 are the gains. The matrix inversion in (15) should not be a problem, because $\det(\hat{T}) = 1$ meaning that $\hat{T}^{-T}$ is always nonsingular regardless of the value of $\hat{\rho}_t$. Consider the parameter update law

$$\dot{\hat{\rho}} = -\Gamma Y^T s, \tag{17}$$

where $Y(\dot{v}, v, \theta, \tau_S, \tau_M) = [\ Y_s \quad -Y_t\ ]$, $\rho^T = [\ \rho_s^T \quad \rho_t^T\ ]$, and Γ > 0 is the gain matrix. In the following, the stability of the control error $\tilde{\theta} = \theta_d - \theta$ will be investigated.

Therorem. 1. The control law (15) together with the parameter update law (17) ensure the following properties: $\tilde{\theta}, s \in \mathcal{L}_2 \cap \mathcal{L}_\infty$, and $\hat{\rho} \in \mathcal{L}_\infty$ where $\mathcal{L}_\infty$ and $\mathcal{L}_2$ stand for the space of bounded and square integrable signals, respectively.

Proof: Substituting the control signal (15) in the system dynamics (13) yields the error dynamics described by

$$\begin{aligned} M_R\dot{s} + C_R s + Ls &= Y_s(\dot{v}, v, \theta, \tau_S)\tilde{\rho}_s - \tilde{T}^T\tau_M \\ &= Y_s(\dot{v}, v, \theta, \tau_S)\tilde{\rho}_s - Y_t(\theta, \tau_M)\tilde{\rho}_t \\ &= Y(\dot{v}, v, \theta, \tau_S, \tau_M)\tilde{\rho}, \end{aligned} \tag{18}$$

Here we have used the property that for any dimensionally compatible vector *x*,

$$T(\theta, \rho_t)x = Y_t(\theta, x)\rho_t,$$

Introducing the positive storage function

$$V = \frac{1}{2}s^T M_R s + \frac{1}{2}\tilde{\rho}^T\Gamma^{-1}\tilde{\rho}$$

and differentiating it along with trajectories of the error dynamics and using Remark 1 yields

$$\dot{V} = -L\|s\|^2 \leq 0. \tag{19}$$

From this, a standard argument (Ioannou and Sun, 1996) proves the theorem.

6.2 Asymptotic Stability

Asymptotic stability of control error $\tilde{\theta}$, or s, can be ensured provided that s is uniformly continuous, i.e., $\dot{s}$ is bounded. The latter can be inferred only if control input τ_M is bounded. The condition for boundedness of τ_M is obtained in the following. For simplicity in presentation we assume that kinematics parameter vector ρ_t is known and then we can derive a simple condition for boundedness of τ_M. Extending results to the case where ρ_t is unknown is straight forward.

Following the Lagrangian approach in (Luca and Lucibello, 1998), the joint torque can be computed from

$$M_L'\ddot{\theta} + h_L(\theta, \dot{\theta}) + d(t) = \tau_J, \tag{20}$$

'where $M_L' = M_L + D^T N^{-1} J$, $M_L \in \mathbb{R}^{n\times n}$ is link inertia matrix, $h_L \in \mathbb{R}^n$ contains all the nonlinear terms, and vector $d(t) \in \mathbb{R}^n$ captures the effect of all external force disturbances

Eliminating the joint accelerations from equations (13) and (20) and solving the resultant equation in terms of τ_S yields

$$\tau_S = \alpha^{-1} R \tau_M + g_1 - \alpha^{-1}\beta, \tag{21}$$

where $R \triangleq M_L'(M_L' + JT)^{-1}$, and $g_1 = (I - R)(h_L + d) - R(h_R + b)$. Substituting τ_S from (12)into (15) gives an expression for the control input independent of τ_S. That is

$$\tau_M = (I - \breve{\alpha}R)^{-1}\, g_2(\dot{v}, v, \dot{\theta}, \theta, \hat{\rho}), \tag{22}$$

where $g_2 = T^{-T}(\hat{M}_R\dot{v} + \hat{C}_R v - Ls) + \hat{\tau}_F + \hat{\alpha}g_1 + \hat{\beta} - \breve{\alpha}\beta$, and

$$\breve{\alpha} \triangleq \mathrm{diag}\{\hat{\alpha}_i/\alpha_i\}$$

˘is the normalized estimation of torque sensor gain. Since all variables of function $g_2(\dot{v}, v, \dot{\theta}, \theta, \hat{\rho})$ are bounded, then $\|g_2\|$is bounded too. Hence, we can say τ_M is bounded if and only if $I - \breve{\alpha}R$ is invertible, i.e.

$$\begin{aligned} \tau_M \in \mathcal{L}_\infty \quad &\Leftrightarrow \quad \lambda_i(I - \breve{\alpha}R) \neq 0 \quad \forall i \\ &\Leftrightarrow \quad \lambda_i(\breve{\alpha}R) \neq 1 \qquad \forall i \\ &\Leftrightarrow \quad \{\theta, \breve{\alpha}\} \notin \mathcal{S}(\theta, \breve{\alpha}), \end{aligned}$$

where

$$\mathcal{S} = \bigcup_{i=1}^{n} \{\theta, \breve{\alpha} | \lambda_i(\breve{\alpha}R(\theta)) = 1\}. \tag{23}$$

Therefore, the control input τ_M remains bounded and the control error $\tilde{\theta}$ asymptotically converges to zero if this part of the system states $\{\theta, \breve{\alpha}\}$α} does not enter the region $\mathcal{S}$. In this case, $\dot{s}$ is bounded and hence s converges asymptotically to zero, which, in turn, implies convergence of $\tilde{\theta}$ to zero.

In the following, we derive a sufficient condition on the gain sensor estimate to achieve a bounded control input.

Remark 2 *Using norm properties, we can obtain a conservative condition satisfying (23) as follows*

$$\begin{aligned} \tau_M \in \mathcal{L}_\infty \quad &\Leftarrow \quad \bar{\sigma}(\breve{\alpha}R) < 1 \\ &\Leftrightarrow \quad \max|\breve{\alpha}_i| < 1/\bar{\sigma}(\mathcal{Q}). \end{aligned} \tag{24}$$

Therefore, joint torques remain bounded providedthat an over-estimation ofthe sensor-gains does not exceed $1/\bar{\sigma}(R)$. Let us choose constant $\bar{\alpha}_i > 0$ so that $\bar{\alpha}_i \geq |\alpha_i|/\bar{\sigma}(R)$ always holds. Then, by virtue of Remark 2, one can show (24) is satisfied if

$$|\hat{\alpha}_i| \leq \bar{\alpha}_i. \tag{25}$$

Based on the projection adaptation law (Ioannou and Sun, 1996), it is possible to modify the parameter update law (17) to ensure that inequality (25) holds. Assume that α_i and ψ_i be the ith elements of $\hat{\rho}$ and $-\Gamma Y^T$ s, respectively. Then, consider the following projection parameter adaptation law for ˆ

$$\dot{\hat{\alpha}}_i = \begin{cases} \psi_i & \text{if} \quad |\hat{\alpha}_i| < \bar{\alpha}_i \ \text{ or} \\ & \quad |\hat{\alpha}_i| = \bar{\alpha}_i \ \text{ and } \ \mathrm{sgn}(\bar{\alpha}_i\psi_i) < 0 \\ 0 & \text{otherwise} \end{cases}$$

A standard argument (Ioannou and Sun, 1996) shows that the modified parameter update law guarantees (25), while keeping (19) negative, i.e. $\dot{V} \leq -L\|s\|$

7. Joint Torque Feedback in the Presence of Actuator Dynamics

Ideally, positive joint torque feedback decouples the load dynamics exactly and provides infinite stiffness for external torque disturbance. This can be possible if an ideal actuator reproduces the same torque as measured by the torque sensor and hence the load torque can be trivially compensated. However, in practice, due to actuator's finite bandwidth dynamics, the feedback system may not respond fast enough to the measured load-torque. As a result, a complete compensation of disturbance torque cannot be achieved in the presence of actuator dynamics and/or delay. This section presents an optimal filter for positive joint torque feedback control which takes the actuator's dynamics into account and minimizes the servo-controller sensitivity to load torque disturbance (Aghili *et al.*, 2001). We show that finding optimal torque feedback is equivalent to the model-matching problem that has an exact solution (?). In the case of dynamic load, optimal torque feedback minimizes the effect of load perturbation on the nominal rotor dynamics. A single variable case is considered herein, yet the analytic solution can be readily extended for a multi-variable case.

7.1 Optimal JTF Design

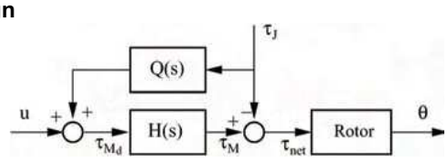

Fig. 8. Joint torque feedback through filter Q(s).

Fig.8 illustrates the general block diagram of a JTF system, where transfer function H(s) represents the actuator dynamics and Q(s) is a filter. The external disturbance τ_J is measured via a torque sensor and the torque signal is fed back for compensation through the filter Q(s). Let u(s)be the compensated control input under positive joint torque feedback in the Laplace domain. Similar to (10), we can define the compensated control input u as

$$\tau_{M_d}(s) = Q(s)\tau_J(s) + u(s), \tag{26}$$

where s is the Laplace variable. The disturbance sensitivity function

$$\chi(s) \triangleq \frac{\tau_{\text{net}}(s)}{\tau_J(s)} = -1 + H(s)Q(s). \tag{27}$$

shows how the disturbance τJ(s)is transmitted to the net torque τnet(s) acting on the rotor. Note that for ideal actuator, where $H(s) = 1$, we can achieve complete decoupling of the disturbance, i.e., $\chi(s)=0$, by trivially choosing $Q(s) =1$.
Also, let $G(s)$ represent the compliance of a position feedback controller, i.e.

$$G(s) = \left.\frac{\partial\theta(s)}{\partial\tau_J(s)}\right|_{Q=0}.$$

Then, one can show that addition of the JTF loop changes the overall compliance of the motion servo to

$$G_{\text{JTF}}(s) = \chi(s)G(s),$$

which is equivalent to the weighted disturbance function (Aghili *et al.*, 2001), if the weighting function is chosen as $W_1(s) = |G(s)|/\|G\|_\infty$.Now, the problem is to finda stable and realizable filter $Q(s) \in \mathcal{RH}$ (the class of H_∞ functions which are rational) such that the maximum weighted sensitivity of the system is minimized, that is

$$\inf_{Q(s)\in\mathcal{RH}} \left\| \begin{bmatrix} W_1(1-HQ) \\ W_2Q \end{bmatrix} \right\|_\infty . \tag{28}$$

Note that the first weighting function, $W_1(s)$, shapes the disturbance gain over frequency band of interest, while the second weighting function, $W_2(s)$, shapes the magnitude of the optimal filter Q(s). Note that $W_2(s)$ causes the magnitude of the torque filter Q(s) is rolled off at high frequency where the magnitude of $W_1(s)$ is sufficiently low. Problem (28) is a standard H_∞ problem and the optimal solution is available.

7.2 Experimental Results

This section evaluates the performance of the proposed JTF experimentally in terms of torque disturbance attenuation and position tracking accuracy under varying payload. In order to measure the torque disturbance sensitivity, torque disturbances are directly injected into the a joint-servo system by using a hydraulic dynamometer. Also, an arm with adjustable payload is mounted on the motor's shaft to investigate the load decoupling and robust stability properties.

7.3 Setup

Fig. 9 illustrates the experimental setup which consists of the McGill/MIT Direct-Drive electric motor (Aghili *et al*., 2002b) mounted on the dynamometer, instrumented with our custom torque sensor described in Section 4, and coupled to a hydraulic rack and pinion rotary motor (Parker 113A129BME). The role of the hydraulic motor is to generate a random disturbance torques in order to measure the disturbance sensitivity of the servo controller.

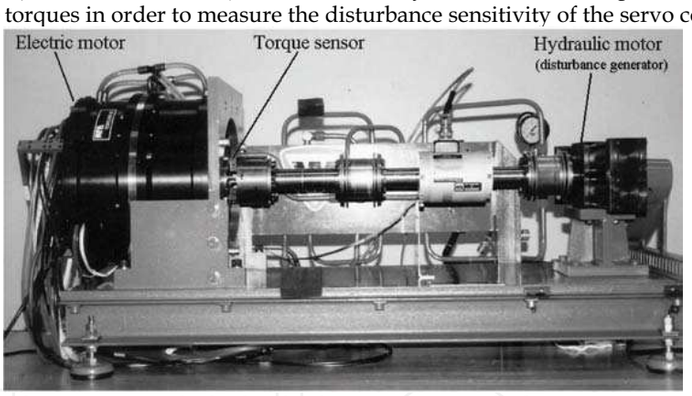

Fig. 9. Direct-drive motor on the hydraulic dynamometer testbed.

7.4 Identification

The performance of joint torque feedback critically relies on the knowledge of actuator dynamics, that, in turn, can be obtained form disturbance sensitivity tests. Let us consider again the control system shown in Fig. 8.The challenge in identification system $H(s)$ is that signal τ_M is not me asurable. How-ever, the actuator transfer function can be extracted from measurements of the disturbance sensitivity functions with respect to two different torque feedbacks. Denoting G_{JTF} as the sensitivity function corresponding to $Q \equiv 1$, one can obtain $G'_{\mathrm{JTF}}(s) = (H(s)-1)G(s)$ from (27). Let us assume that $\Phi_{\tau_J\tau_d}$ and $\Phi'_{\theta\tau_J}$ denote the corresponding spectral τ_J densities when $Q = 1.$. Then, one can obtain the empirical (non-parametric) transfer function $\hat{H}(\omega)$ from the latest equation as

$$\hat{H}(j\omega) = 1 + \frac{\Phi_{\theta\tau_J}(j\omega)\Phi'_{\tau_J\tau_J}(j\omega)}{\Phi'_{\theta\tau_J}(j\omega)\Phi_{\tau_J\tau_J}(j\omega)}. \tag{29}$$

The next step of the identification involves a numerical procedure to represent the complex function (29) by a rational transfer function as close as possible .Several parametric models were examined, and it turned out that a second order systems is sufficient to match the input-output behavior adequately. The parametric models approximating *G* (jω) and *H* (jω), which are used for the feedback design, are

$$\hat{G}(j\omega) \approx \frac{-0.002s + 0.226}{s - 9.523}, \quad \text{and} \quad \hat{H}(j\omega) \approx \frac{-5.014s + 578}{s^2 - 35.59s + 604}.$$

Note that $\hat{H}(j0) = 0.96$ represents the DC gain of the actuator.

7.5 Disturbance Rejection Tests

We compare the disturbance attenuation of our servo controller with and without using JTF. To this end, we command a ramp reference signal through the PID position controller while the hydraulic motor injects random torque disturbances. Fig. 10 illustrates the position tracking error trajectories due to the random torque disturbances without and with the torque feedback is applied. The control system exhibits relatively high disturbance sensitivity when there is no torque feedback. The figure clearly shows that the tracking error is substantially reduced when the torque feedback is applied. The disturbance attenuation is better explained in Fig. 11 in the frequency domain. As expected, at a sufficiently high frequency, the disturbance sensitivity drops due to the attenuation effect of position feedback. The torque feedback lowers this system sensitivity remarkably over the whole frequency range.

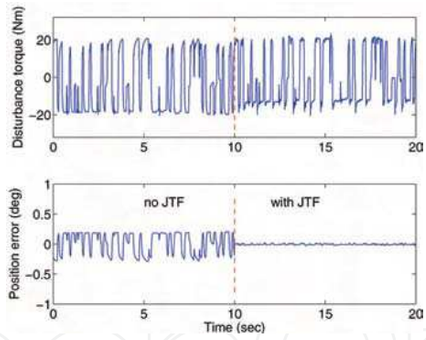

Fig. 10. Tracking error with and without JTF is applied.

due to the random torque disturbances without and with the torque feedback is applied. The control system exhibits relatively high disturbance sensitivity when there is no torque feedback. The figure clearly shows that the tracking error is substantially reduced when the torque feedback is applied. The disturbance attenuation is better explained in Fig. 11 in the frequency domain. As expected, at a suciently high frequency, the disturbance sensitivity drops due to the attenuation effect of position feedback. The torque feedback lowers this system sensitivity remarkably over the whole frequency range.

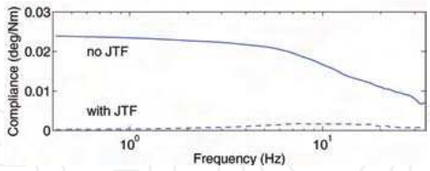

Fig. 11. Disturbance attenuation with and without JTF is applied.

The next objective is to demonstrate experimentally the performance of the servo controller with JTF under a dynamical load. To this end, a link with a 7.2 kg mass is mounted on the motor's torque sensor that plays the role of an uncertain payload. The counterbalance weight produces a nonlinear gravity torque to be compensated with positive joint torque feedback. To investigate the tracking performance of the control system, we commanded a sinusoidal reference position trajectory θ_d (t) = π/4cos (πt/3) rad to the motion controller. First, no JTF is applied. Since the nonlinear link dynamics (due to the gravitational term) are not compensated by a JTF controller, the tracking error resulting from the PID controller alone is large, as shown in Fig. 12. Yet, when the joint torque feedback is applied the tracking error is reduced significantly.

Sensor Type	Sensitivity mV/Nm	Torsional Stiffness 10^4 Nm/rad	Bending Stiffness 10^4 Nm/rad	η 10^3 V/rad
B	45.7	3.4	N/A	1.55
C	96.5	1.5	N/A	1.45
E	30	24	480	7.2

Table 1. A comparison with various type of torque sensors.

8. Conclusion

Motivated by the need for accurate joint torque sensing in robots, we designed a new torque sensor, based on the hollow hexaform geometry. Its key features were its extremely high stiffness and its insensitivity to the set of support forces and moments which persist in a robot joint. These features permit to mount the sensor directly in the joints of a robot manipulator leading to accurate joint torque sensing and to a compact and modular design. The structure of the sensor also exhibits strain concentration to torsion loads which maximizes the sensitivity to torsion without sacrificing torsional stiffness. Other design issues such as practical shape consideration, material properties and overloading also considered. The sensor geometry was analyzed and optimized using the finite element method. The sensor was tested extensively to confirm its design goals, and is well suited as a torque-sensing device in robots or other industrial high performance motion control applications. A quantitative comparison with different types of sensors is shown in table 1. The table indicates that our sensor's performance characteristics compare very favorably.

The applications of adaptive control in conjunction with joint-torque sensory feedback was used for dynamic motion control of manipulators. The control system had the advantages of requiring neither the computation of link dynamics nor the precise measurement of joint torques, i.e., the torque sensor's gains and offsets are unknown to the controller. The adaptive controller could also tune all the joint parameters including the rotor inertia, twist

angles of joint axes, and joint friction parameters. The stability of the control system was investigated analytically. It was shown that the control error asymptotically converges to zero if an upper bound on the estimated sensor gain is respected. Subsequently, the parameter update law was modified based on the projection algorithm to satisfy the boundedness condition.

Next, we formulated the problem of optimal positive JTF in the presence of actuator's finite bandwidth dynamics. The theory of JTF was further developed to suppress the effect of load torque disturbance on a motion control systems in the presence of actuator dynamics. An experimental setup comprised of a direct-drive electric motor, torque-sensor, and hydraulic motor was constructed to measure disturbance sensitivity of a motion servo mechanism. The results demonstrated that when the servo controller was cascaded with the optimal JTF, a significant reduction in sensitivity was achieved. In our second experiment, a single link with adjustable inertia was attached to the motor. In the absence of any torque feedback, the tracking error increased due to load nonlinearity, and increases with payload, while the optimal feedback maintains the tracking accuracy.

9. References

Aghili, F. and M. Namvar (2006). Adaptive control of manipulator using uncalibrated joint-torque sensing. IEEE Trans. Robotics 22(4), 854-860.

Aghili, F., M. Buehler and J. M. Hollerbach (2002a). Design of a hollow hexaform torque sensor for robot joints. *Int. Journal of Robotics Research* 20(12), 967 –976.

Aghili, F., M. Buehler and J. M. Hollerbach (2002b). Development of a high performance joint. *Int. Journal of Advanced Robotics* 16(3), 233–250.

Aghili, Farhad, Martin Buehler and John M. Hollerbach (2001). Motion control systems with h-infinity positive joint torque feedback. *IEEE Trans. Control Systems Technology* 9(5), 685–695.

An, C. H., C. G. Atkeson and J. M. Hollerbach (1988). *Model-Based Control of a Robot Manipulator*. MIT Press. Cambridge, MA.

Asada, H. and S.-K. Lim (1985). Design of joint torque sensors and torque feedback control for direct-drive arms. In: *ASME Winter Annual Meeting: Robotics and Manufacturing Automation*, PED-Vol. 15. Miami Beach. pp. 277–284.

de Wit, C. Canudas, H. Olsson, K. J. Aström and P. Lischinsky (1995). A new model for control of systems with friction. *IEEE Transactions on Automatic Control* 40(3), 419–425.

deSilva, C. W., T. E. Price and T. Kanade (1987). Torque sensor for direct-drive manipulator. *ASME Journal of Engineering for Industry* 109, 122–127.

Hashimoto, M. (1989a). Robot motion control based on joint torque sensing. In: Proc. *IEEE Int. Conf. Robotics and Automation.* pp. 256–1261.

Hashimoto, M. (1989b). Robot motion control based on joint torque sensing. In: *IEEE Int. Conf. Robotics and Automation.* pp. 256–261.

Hirose, S. and K. Yoneda (1990).Development of optical 6-axial force sensor and its signal calibration considering non-linear interference. In: Proc. *IEEE Int. Conf. Robotics and Automation.* Cincinnati. pp. 46–53.

Hirzinger, G., A Albu-Sc¨ahnle, I. Schaefer and N. Sporer (2001). On a new generation of torque controlled light-weight robots. In: *IEEE Int. Conf. On Robotics & Automation*. Seoul, Korea. pp. 3356–3363.

Ioannou, P. A. and J. Sun (1996). *Robust Adaptive Control*. Prentice Hall. New Jersey.

Jacobsen, S.C., F.M. Smith, D.K. Backman and E.K. Iversen (1991). High performance, high dexter ity, force reflective teleoperator ii. In: *ANS Topical Meeting on Robotics and Remote Systems*. Albuquerque, NM. pp. 24–27.

Kosuge, K., H. Takeuchi and K. Furuta (1990). Motion control of a robot arm using joint torque sensors. *IEEE Trans. Robotics and Automation* 6(2), 258–263.

Lebow (1997).Lebow load cell torque sensor handbook. Technical Manual 710.Eaton Corporation, Lebow Products. Troy, Michigan 48099, USA.

Lozano, R. and B. Brogliato (1992). Adaptive control of robot manipulators with flexible joints. *IEEE Trans. on Automatic Control* 37(2), 174–181.

Luca, A. De and P. Lucibello (1998). A general algorithm for dynamic feedback linearization of robots with elastic joints. In: *IEEE Int. Conf. On Robotics & Automation*. Leuven, Belgium. pp. 504– 510.

Luh, J. Y. S., M. W. Walker and R. P. Paul (1980). Resolved acceleration control of mechanical manipulator. *IEEE Trans. Automatic Control* 25(3), 468–474.

Luh, J.Y.S, W.D. Fisher and R.P.C. Paul (1983). Joint torque control bya direct feedback for industrial robot. *IEEE Trans. Automatic Control* 28, 153–161.

Murphy, S. H., J. T. Wen and G. N. Saridis (1990). Simulation and analysis of flexibly jointed manipulators. In: 29 *Th IEEE Conf. On Decision and Control*. Honolulu, HI. pp. 545–550.

Newman, W. S. and J. J. Patel (1991). Experiments in torque control of the adept-one robot. In: Proc. *IEEE Int. Conf. Robotics and Automation*. pp. 1867–1872.

Omega (1995).The pressure strain and force handbook. Technical Manual 29.OMEGA. Stamford, CT 06907-0047, USA.

Pfeffer, L. E., O. Khatib and J. Hake (1989). Joint torque sensory feedback in the control of a puma manipulator. *IEEE Trans. Robotics and Automation* 5(2), 418–425.

Reed, J. S. and P. A. Ionnou (1989). Instability analysis and robust adaptive control of robotic manipulator. *IEEE Trans. on Robotics and Automation* 5(3), 381–386.

Sciavicoo, L. and B. Siciliano (2000). *Modeling and Control of Robot Manipulator*. 2 ed.. Springer.

Slotine, J. J. E. (1985). The robust control of manipulators. *Int. J. of Robotics Research* 4(2), 49–64.

Slotine, J. J. E. and W. Li (1987). On the adaptive control of robot manipulators. *Int. J. of Robotics Research* 6(3), 49–59.

Spong, M. W. (1987). Modelingandcontrol of elastic joint robots. Transactions of the *ASME Journal of Dynamic Systems, Measurement, and Control* 109, 310–319.

Stokic, Dragan and Miomir Vukobratovic (1993). Historical perspectives and states of the art in joint force sensory feedback control of manipulation robots. *Robotica* 11, 149–157.

Svinin, M.M. and M. Uchiyama (1995). Optimal geometric structures of force/torque sensors. *The International Journal of Robotics Research* 14(6), 560–573.

Tani, Y., Y. Hatamura and T. Nagao (1983).Development of small three component dynamometer for cutting force measurement. *Bulletein of the JSME.*

Techniques, Transducer (n.d.). Load cell transducer. Technical manual. Transducer Techniques. 43178T Business Park Dr., CA 92590 (NR).

Tomei, P. (1991).A simple PD controller for robots with elastic joints. *IEEE Trans. on Automatic Control* 36, 1208–1213.

Uchiyama, M., E. Bayo and E. Palma-Villalon (1991). A systematic design procedure to minimize a performance index for robot force sensors. *Journal of Dynamic Systems, Measurement, and Control* 113, 388–394.

Vischer, D. and O. Khatib (1995). Design and development of high-performance torque-controlled joints. *IEEE Trans. Robotics and Automation* 11, 537–544.

Wu, C-H. (1985). Compliance control of a robot manipulator based on joint torque servo. *The International Journal of Robotics Research* 4(3), 55–71.

Wu, C-H. and R.P. Paul (1980). Manipulator compliance based on joint torque control. In: Proc. *IEEE Int. Conf. Decision and Control*. pp. 88–94.

Yong-Duan, S., G. Wei-Ningand C. Mian (1989). Studyon path tracking control of robot manipulators with unknown payload. In: *IEEE Int. Conf. On System Eng.* Fairborn, OH. pp. 321–324.

Zhang, G. and J. Furusho (1998). Control of robot arms using joint torque sensors. *IEEE Control systems* 18(1), 48–54.

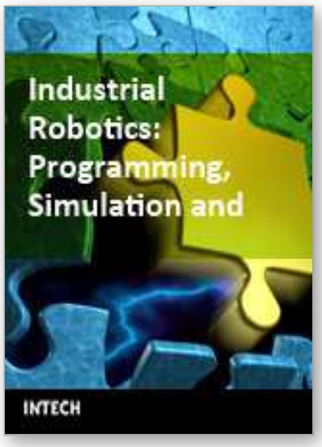

Industrial Robotics: Programming, Simulation and Applications

Edited by Low Kin Huat

ISBN 3-86611-286-6

Hard cover, 702 pages

Publisher Pro Literatur Verlag, Germany / ARS, Austria

Published online 01, December, 2006

Published in print edition December, 2006

This book covers a wide range of topics relating to advanced industrial robotics, sensors and automation technologies. Although being highly technical and complex in nature, the papers presented in this book represent some of the latest cutting edge technologies and advancements in industrial robotics technology. This book covers topics such as networking, properties of manipulators, forward and inverse robot arm kinematics, motion path-planning, machine vision and many other practical topics too numerous to list here. The authors and editor of this book wish to inspire people, especially young ones, to get involved with robotic and mechatronic engineering technology and to develop new and exciting practical applications, perhaps using the ideas and concepts presented herein.

InTech Europe

University Campus STeP Ri
Slavka Krautzeka 83/A
51000 Rijeka, Croatia
Phone: +385 (51) 770 447
Fax: +385 (51) 686 166
www.intechopen.com

InTech China

Unit 405, Office Block, Hotel Equatorial Shanghai
No.65, Yan An Road (West), Shanghai, 200040, China
中国上海市延安西路65号上海国际贵都大饭店办公楼405单元
Phone: +86-21-62489820
Fax: +86-21-62489821

IntechOpen